IEEE Access
Multidisciplinary ⋮ Rapid Review ⋮ Open Access Journal

Received 6 April 2024, accepted 27 April 2024, date of publication 21 May 2024, date of current version 30 May 2024.

Digital Object Identifier 10.1109/ACCESS.2024.3403829

RESEARCH ARTICLE

Simultaneous Enhancement of Photovoltaic System Intermittency and Damping Load Variations in Noninverting Buck-Boost Converters Using Robust Weighted Mixed-Sensitivity Control

REZA FAUZI ISKANDAR[1,2], HANADI[1], HARTONO[3], EDI LEKSONO[1], AND ENDRA JOELIANTO[4], (Senior Member, IEEE)

[1]Department of Engineering Physics, Faculty of Industrial Technology, Institut Teknologi Bandung, Bandung 40132, Indonesia
[2]Department of Engineering Physics, School of Electrical Engineering, Telkom University, Bandung 40257, Indonesia
[3]Department of Instrumentation and Control, Faculty of Industrial Technology, Institut Teknologi Bandung, Bandung 40132, Indonesia
[4]Instrumentation, Control, and Automation Research Group, Faculty of Industrial Technology, Institut Teknologi Bandung, Bandung 40132, Indonesia

Corresponding author: Edi Leksono (leksono@itb.ac.id)

This work was supported by Lembaga Pengelola Dana Pendidikan (LPDP) under Grant KET-5154/LPDP.3/2023, The Ministry of Finance, Republic of Indonesia through Indonesian Education Scholarship Program.

ABSTRACT Due to the intermittent and uncertain nature of photovoltaic systems, their incorporation within a DC microgrid presents a challenge to primary control, which directly interfaces with the generation converter. By utilizing a weighted mixed sensitivity control, this study aims to amplify the robustness of a noninverting buck-boost converter integrated photovoltaic system in addressing the uncertainties and disturbances arising from simultaneous fluctuations in irradiance, temperature, and load. The robust control algorithm was formulated by employing frequency-weighting functions and imposing a requirement for the minimum norm of the transformation matrix to achieve robust performance and robust stability. Furthermore, the involvement of reference models in a robust control synthesis offered additional advantages in enhancing the damping of the system. Consequently, the entire design configuration could effectively establish the converter robustness against both generation and load intermittencies occurring simultaneously. The simulation and experiment results are demonstrated to illustrate the efficiency of the designed algorithm.

INDEX TERMS Robust control, weighted mixed-sensitivity, noninverting buck-boost converter, photovoltaic system, voltage tracking, maximum power point.

I. INTRODUCTION

Control and optimization are key factors in improving the operational efficiency of off-grid photovoltaic (PV) systems, which involve input and output intermittence. The off-grid structure offers several significant advantages in various aspects. One of the main benefits is higher efficiency, particularly because it is located in one place. This avoids the energy loss impact that typically occurs due to long-distance transmission when connected to the grid, especially in remote areas. Another notable advantage is the absence of emissions, which is because these systems do not require conventional energy as a backup [1], [2]. However, it must be acknowledged that there are several issues that need to be addressed. One of these issues is the complexity and sensitivity of switching mechanisms among various green energy sources and energy storage [3]. This is necessary to ensure efficient and reliable operation, considering the deep cycle of batteries for frequency regulation and grid stabilization. Another challenge that arises in off-grid structures is the

The associate editor coordinating the review of this manuscript and approving it for publication was Jinquan Xu.

absence of support for reactive power. This poses a challenge because photovoltaic systems essentially generate only active power [4], while equipment typically requires AC power with reactive power characteristics [5]. By addressing these constraints, off-grid systems can ensure sustainability and efficiency, thus contributing significant benefits, especially in remote areas that are not easily accessible by conventional grids.

Photovoltaics are predicted to become a promising energy supply in the future [6], [7]. However, the variability and unpredictability of electrical characteristics produced by photovoltaic systems introduce distinctive difficulties, arising from the fluctuations and disruptions they exhibit. The high PV penetration can cause serious imbalances [8], increase excessive currents [9], and disrupt the transient stability of the system [10]. Factors such as cloud movements, temperature, shading, and electrical load variation can negatively impact the performance and reliability of PV systems, and are also counterproductive to their efficiency. To solve these problems, addressing fluctuations and disturbances in the control design of PV systems is crucial for ensuring performance efficiency and stability [11]. Moreover, facing this situation, the controller must be able to achieve the maximum power point (MPP) of the photovoltaic module.

Various control innovations for DC/DC converter integrated photovoltaic system applications can be found in several studies. Naghmash et al. [12] designed a nonlinear control for MPPT incorporated alongside a noninverting buck-boost converter through the backstepping method approach. Mendez-Diaz et al. [13] developed a buck-boost converter with a sliding mode control strategy in photovoltaic applications to ensure a smooth transition between the buck and boost modes. Cabrane et al. [14] proposed a new dimension for a PI controller aimed at voltage bus stabilization through a buck-boost converter linked to a battery and supercapacitor unit, while also incorporating photovoltaic-based generation connected to a boost converter employing a similar control approach. Restrepo et al. [15] successfully implemented a switching frequency mechanism in the current loop using a model predictive control algorithm approach.

Obeidi et al. [16] employed a PV system integrated with a buck-boost converter using direct control strategy to pursue the global MPP. The performance evaluation indicates that the approach can accurately yield the global MPP with high speed while reducing implementation costs. Iskandar et al. [17] performed preliminary studies to mitigate solar irradiation fluctuations in photovoltaic systems based on buck-boost converter using a Q-learning integrated type-2 fuzzy control strategy. Furthermore, in the context the of buck-boost converter principle, which that works to regulate an adjustable output voltage, regardless of the input voltage, switching between buck mode and boost mode allows flexible voltage settings according to system needs. Systems that combine two or more modes of system models or controllers are known as hybrid systems [18], [19], [20]. Specifically, hybrid systems are combinations and interactions of discrete and continuous systems or different types of mathematical models [21], [22], [23]. Robust controllers have demonstrated their effectiveness in controlling hybrid systems [24], [25], [26], [27].

It is essential to note that the synthesis of the above method becomes valid due to the availability of mathematical equations for the system. However, in industrial applications, a perfect physical model of the system may not always be attainable [28]. This limitation is primarily attributed to factors such as uncertainty, complexity, nonlinearity, and the presence of various disturbances. In a photovoltaic system, uncertainty can be present within each subsystem and can have a negative impact on the system's performance [29], such as the uncertainty in the electronic components of the DC/DC converter, input voltage level, and load variation [30]. This system is susceptible to the influence of disturbances, which may pose challenges for the controller in achieving optimal performance [31], such as for the current and voltage of photovoltaic systems, where their values depend on adjustments in solar irradiance and environmental temperature. In a short span of time, the voltage can dramatically shift due to abrupt weather changes and load variations, consequently leading to disruptions in the system. Robust control has the potential to address these issues simultaneously. We can design a weight function in such a way that the output is less sensitive to disturbances [32]. The closed-loop system performance can be augmented with a weight function over the range of system disturbances and component uncertainties, thereby enabling the controller to ensure closed-loop stability, good performance, and robustness [33].

The applications of robust control in power electronics can be found in various studies. Hiti et al. [34] published a study on robust nonlinear control for a boost converter, with the design objective aimed at eliminating the controller's sensitivity to changes in the magnitude of resistive load variations. Buso et al. [35] successfully applied the voltage control of a buck-boost converter using a singular value approach, considering the tolerance of the reactive component and operational point variations. Hernandez et al. [36] implemented H_∞ loop-shaping on a buck-boost converter, specifically where the control design was applied to ensure robust stability in the presence of disturbances. Joelianto and Tommy [37] proposed a robust controller for a buck-boost converter using the H_∞ optimization technique in PID parameterization. Sitbon et al. [38] innovated a simplified control reduction in the form of an op-amp through robust control synthesis. This approach addresses issues such as control burden and environmental variable interference. Gandini et al. [39] investigated robust control architectures to address the issue of thermoelectric generator instability due to temperature fluctuations while simultaneously improving the efficiency of the noninverting buck-boost converter.

Cortes-Vega et al. [40] proposed robust control for a PV system incorporated alongside a buck-boost converter

using an attractive ellipsoid approach to determine the MPP. Keskin et al. [41] proposed control technique for a two-leg interleaved boost converter-based input voltage feed-forward (IVFF) approach using a robust fixed-order H_∞ and a resulting low order controller. This method addresses fluctuations in load current and input voltage perturbations, which were confirmed in both experimental and simulation environments. The authors reported a 40 ms convergence time without causing oscillation or overshoot. Another innovation related to H_2/H_∞ framework synthesis for a static synchronous compensator to enhance the damping power network oscillation problem was created by Devarapalli et al. [42]. They utilized the whale optimization algorithm and particle swarm optimization to enhance the power system stabilizer to ensure proper controller design. In reference to the papers above, disturbance suppression and model uncertainty issues are the primary focus of robust control design in addressing the dynamics issue of power converters.

In light of the literature, the design of robust weighted mixed-sensitivity control systems involving reference models concerning a noninverting buck-boost converter integrated with photovoltaics has not been extensively explored. The presence of a reference model provides additional advantages in improving system performance because it can serve as a reference for how the ideal system response works. It is important to anticipate the disturbance aspects that arise from photovoltaic voltage fluctuations, which result from variations in irradiance, environmental temperature, and load. This situation can be mitigated by incorporating filters in the synthesis of weighted mixed-sensitivity control to minimize disturbance sensitivity to the output. Furthermore, the issue of model parameter uncertainty is also one of the considerations in control design, so that the entire design configuration can establish converter robustness against intermittencies from both the generation and load sides simultaneously.

The urgency of related issues can be specifically examined in several studies related to the development of control systems for off-grid photovoltaics integrated with DC converters. Some of these works provide solutions to address intermittency from the PV generator side, load side, and their combination. Verification through simulations, experiments, and their combination is also included in the report. The development of control for off-grid photovoltaics facing changing irradiance conditions was reported by Farag et al. [43]. The photovoltaic system interfaces with a boost converter to handle sudden irradiance fluctuations using an optimized fractional nonlinear synergic controller. The experimental results were reported under varying irradiance and constant load conditions. Furthermore, Cortes-Vega et al. [40] employed the attractive ellipsoid robust control approach to create robust maximum power point tracking (MPPT) in a photovoltaic system integrated with a noninverting buck-boost converter. Validation was conducted through simulation under changing temperature and irradiance conditions as well as under a constant load. The system's performance is claimed to exhibit fast convergence and low oscillation. Kchaou et al. [44] implemented a strategy for boosting converters in a photovoltaic system using a second-order sliding mode-based MPPT approach. The validation was conducted through simulation under varying irradiance and temperature test conditions.

Other researchers have reported irradiance variation and load conditions as presented by Shams et al. [45], who proposed an MPPT improvement using the social ski driver method on a photovoltaic system integrated with a buck-boost converter system. The system was validated under changing irradiance and load conditions with a tracking speed of less than 1 second. Furthermore, the testing conducted under irradiance and constant load conditions, as presented by Callegaro et al. [46], involved designing feedback linearization control (FLC) for a photovoltaic system integrated with a noninverting buck-boost converter with MOSFET gates. FLC is aimed at maintaining the photovoltaic module voltage and average inductor current. The control performance is reported in an experimental setup under varying irradiance and constant load conditions. Additionally, Callegaro et al [47] proposed smooth transfer for a noninverting buck-boost converter and reported successful testing for varying MPPT values and constant loads.

In line with the paper's main objectives and in comparison with related literature, the major contributions of this work can be summarized as follows:

- The proposed strategy is formulated to simultaneously overcome the natural problems in photovoltaic systems related to irradiation and temperature fluctuations, such as disturbance intermittence in the system, model parameter uncertainty, and load variation which disturb system stability.
- Another benefit of the proposed algorithm is that the robust control solution is computationally friendly to implement in microcontroller devices because the control structure is a single function. It is feasible for industrial applications to control the dynamics of noninverting buck-boost converter.
- The objective design and advantages are validated through both simulations and experiments.

The structure of this paper is as follows. The second section describes the modeling of PV systems and the MPP representation. The third section presents the noninverting buck-boost model. The fourth section presents the uncertainty problem in the system model. The robust weighted mixed-sensitivity control strategy is described in the fifth section. The sixth and seventh sections present the simulation and experimental results, respectively, which are summarized in the conclusion in the last section.

II. PHOTOVOLTAIC MODEL AND MPP REGRESSION

Photovoltaic cell technology consists of various solar cells that use solar energy to produce electrical energy. The amount of renewable energy produced by photovoltaic systems depends on the amount of sunlight transmitted daily by

each cell [48], [49]. An ideal photovoltaic system is a series of electrical components consisting of parallel and series resistors, diodes, and photoelectric current produced by a single photovoltaic cell [50]. In the literature, multiple equivalent circuit models are available for simulating photovoltaics. One of the widely recognized models is the equivalent circuit of a single diode. This model was chosen because of its ease of scrutiny [51]. In this model, the diode characteristics represent the conditions under which photovoltaic solar cells are sensitive to sunlight. Because there is a diode current in the photovoltaic cell equivalent circuit, this circuit has nonlinear characteristics. Additionally, this model considers the existence of series and parallel resistors that affect the overall performance of the photovoltaic cell [52]. A photovoltaic model with one diode in an equivalent circuit is shown in Fig. 1 [52].

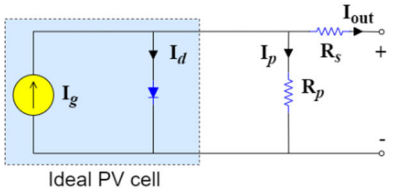

FIGURE 1. Equivalent circuit of photovoltaic devices.

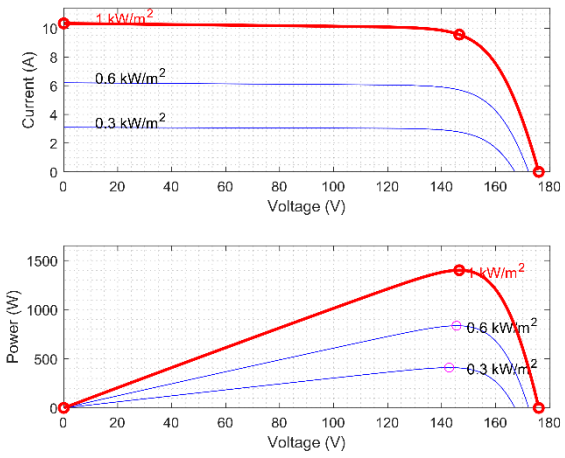

FIGURE 2. Photovoltaic array characteristics.

The photovoltaic model in this equivalent electrical circuit consists of I_g as the current source generated by solar irradiation and I_d as the electric current flowing through the diode. I_p is the electrical current loss through parallel parasitic resistance R_p. The electric current produced by photovoltaics based on Kirchhoff's current law is written as follows.

$$I_{out} = I_g - I_d - I_p \tag{1}$$

where

$$I_d = I_o \left[\exp\left(\frac{q\,(V + R_s I)}{AkT_c} \right) - 1 \right] \tag{2}$$

$$I_p = \frac{V + R_s I}{R_p} \tag{3}$$

I_o, q, A, k, T_c, R_s and R_p show the minimum current passing through the diode when operated in reverse mode, electric charge, diode ideal factor, Boltzmann constant, PV module temperature, series resistance and parallel resistance. If (2) and (3) are substituted into (1), then the current produced by the photovoltaic system can be written as (4) [53].

$$I_{out} = I_g - I_o \left[\exp\left(\frac{q\,(V + R_s I)}{AkT_c} \right) - 1 \right] - \frac{V + R_s I}{R_p} \tag{4}$$

Changes in photovoltaic power are influenced by irradiance and environmental temperature. The P-V curve is used to represent variations in the power characteristics of the PV system. Based on this variability, a reference voltage is needed to achieve an influential maximum power point that undergoes continuous changes over time [54]. The PV characteristic curve is shown in Fig. 2. Furthermore, the voltage at the MPP as a function of irradiance and temperature was obtained at a temperature of 5–75 °C and with irradiance of 200–1,200 W/m^2. Then, a regression field was created to provide a reference voltage. The regression field obtained is shown in Fig. 3.

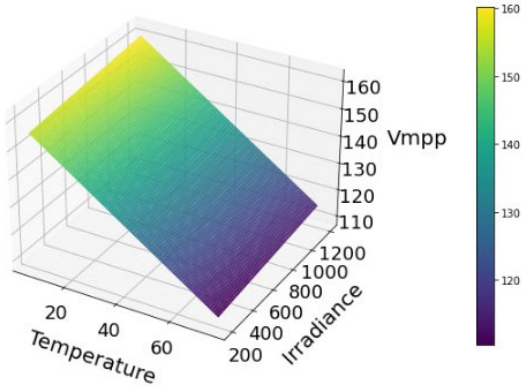

FIGURE 3. Voltage regression for driving MPP.

According to Fig. 3, the equation of the reference voltage v_{ref} to drive the MPP, $v_{ref} = v_{mpp}$, is based on the regression plane in Fig. 3. It is written as follows:

$$\begin{aligned} v_{ref} &= 138.15 - 0.0009 \times \text{Temperature} + 0.03 \times \text{Irradiance} \\ &\quad + 0.00006 \times \text{Temperature}^2 \\ &\quad - 0.0006 \times \text{Temperature} \times \text{Irradiance} \\ &\quad - 0.000009 \times \text{Irradiance}^2 \end{aligned} \tag{5}$$

According to the linear interpolation, the maximum power is then determined based on the PV characteristic curve using the equation below.

$$P = v_{mpp} \times i_{mpp} \tag{6}$$

The maximum power obtained in each condition (300 W/m^2, 25 °C, 600 W/m^2, 25 °C, and 1,000 W/m^2, 75 °C) was approximately 410.44 W, 836.47 W, and 1400.73 W, respectively.

III. NONINVERTING BUCK-BOOST CONVERTER MODELING

The output voltage of the photovoltaic array can be controlled with a noninverting buck-boost converter [55]. Unlike the inverting buck-boost converter, the noninverting buck-boost converter generates an output voltage that aligns with the voltage sign of the input. To achieve its optimal power output, the controlled converter can align the electrical potential of the photovoltaic array with the specified voltage level that corresponds with the MPP. This is accomplished through precise adjustment of the duty ratio [56].

A proficient robust controller can regulate a noninverting buck-boost converter by adjusting the duty ratio to control the switch. Integrating a robust controller enables the creation of an efficient and effective system for regulating the voltage output of a photovoltaic array [57]. The ideal components used include photovoltaic input voltage v_{pv}, capacitors C_α and C_β, diodes D_a and D_b, inductor L, MOSFET switches S_a and S_b, and output voltage v_o. The design considerations for the noninverting buck-boost converter during the continuous conduction mode of operation are depicted in Fig. 4. The output voltage response v_o of the noninverting buck-boost converter to an input from the PV module voltage v_{pv} is shown in Fig. 5. A smooth transition from boost to buck can be observed in the output voltage v_o, where v_o, as a blue line, increases corresponding to a duty cycle > 0.5 in boost mode, and the voltage decreases corresponding to an input duty cycle < 0.5 in buck mode.

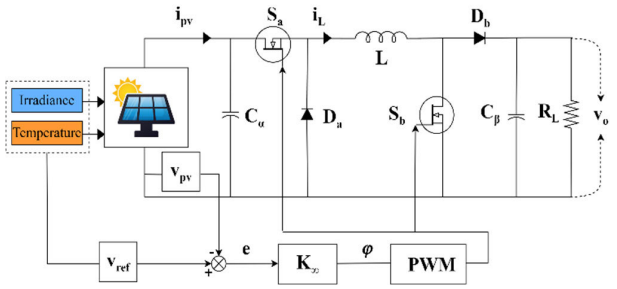

FIGURE 4. Circuit diagram of the noninverting buck-boost converter system with a controller.

In mode 1, both switches S_a and S_b are activated, creating an inductor charging mode as a consequence of the reverse biased condition in diode D_a. Considering Kirchhoff's voltage and current laws in Fig. 6, with this circuit, i_{C_α}, i_{C_β}, and v_L are the capacitor current of C_α, C_β, and the inductor voltage, respectively. These values are $C_\alpha dv_{pv}/dt$, $C_\beta dv_o/dt$, and Ldi_L/dt, respectively. Kirchhoff's current laws give $i_{pv} = i_{C_\alpha} + i_L$ which is expressed in (7):

$$\frac{dv_{pv}}{dt} = \frac{i_{pv}}{C_\alpha} - \frac{i_L}{C_\alpha} \tag{7}$$

In this mode, the voltage across the inductor is equal to the photovoltaic voltage $v_L = v_{pv}$; thus, we express (8).

$$\frac{di_L}{dt} = \frac{v_{pv}}{L} \tag{8}$$

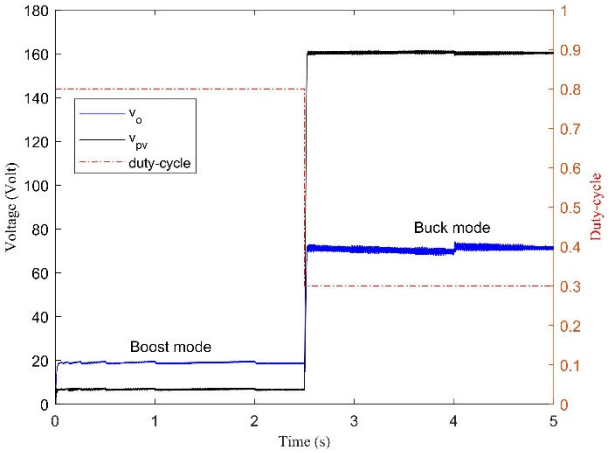

FIGURE 5. Mode transition of noninverting buck-boost converter.

Similarly, the current through the capacitor C_β and the current entering the load satisfy $i_{C_\beta} = -i_R$; thus, we obtain (9).

$$\frac{dv_o}{dt} = -\frac{v_o}{RC_\beta} \tag{9}$$

Furthermore, in mode 2, both switches S_a and S_b are turned off, creating an inductor discharging mode as a consequence of forward bias in diodes D_a and D_b.

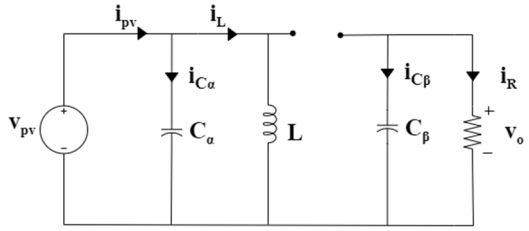

FIGURE 6. Mode 1 of the noninverting buck-boost converter.

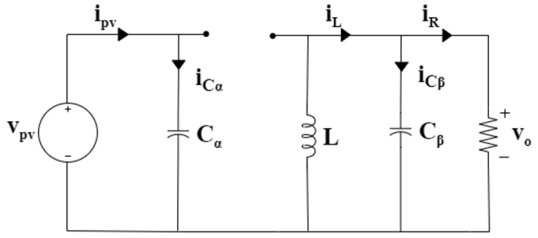

FIGURE 7. Mode 2 of the noninverting buck-boost converter.

Considering Kirchhoff's voltage and current laws in Fig. 7, $i_{C_\alpha} = i_{pv}$ is obtained and can be expressed as in (10).

$$\frac{dv_{pv}}{dt} = \frac{i_{pv}}{C_\alpha} \tag{10}$$

The inductor voltage is equal to the voltage across the output load $v_L = -v_o$. Considering the expression for the inductor

voltage, (11) is obtained.

$$\frac{di_L}{dt} = -\frac{v_o}{L} \tag{11}$$

From the right side current loop $i_L = i_{C_\beta} + i_R$ and considering the capacitor current expression, it is rewritten as (12).

$$\frac{dv_{C_\beta}}{dt} = \frac{i_L}{C_\beta} - \frac{v_o}{RC_\beta} \tag{12}$$

To achieve steady-state, conditions, both the capacitor charge balance and inductor volt-second balance are applied, as described in [58], to Equations (7), (8), (9), (10), (11), (12), and then (13) is collected.

$$\begin{cases} \dfrac{dv_{pv}}{dt} = -\dfrac{i_L}{C_\alpha}\varphi + \dfrac{i_{pv}}{C_\alpha} \\ \dfrac{di_L}{dt} = \dfrac{v_{pv}}{L}\varphi - \dfrac{v_o}{L}(1-\varphi) \\ \dfrac{dv_{C_\beta}}{dt} = \dfrac{i_L}{C_\beta} - \dfrac{v_o}{RC_\beta} - \dfrac{i_L}{C_\beta}\varphi \end{cases} \tag{13}$$

Considering that x_1, x_2, and x_3 are state variables, φ is the control signal, and δ is the disturbance.

$$x_1 = v_{pv}, \quad x_2 = i_L, \; x_3 = v_{C_\beta}, \; \delta = i_{pv} \tag{14}$$

Substituting the state variables into Equations (13) with their derivatives over time, we can rewrite

$$\begin{cases} \dot{x}_1 = -\dfrac{x_2}{C_\alpha}\varphi + \dfrac{\delta}{C_\alpha} \\ \dot{x}_2 = \dfrac{x_1}{L}\varphi - \dfrac{x_3}{L} + \dfrac{x_3}{L}\varphi \\ \dot{x}_3 = \dfrac{x_2}{C_\beta} - \dfrac{x_3}{RC_\beta} - \dfrac{x_2}{C_\beta}\varphi \end{cases} \tag{15}$$

This average state model will be used to track voltage as the peak power reference. Equation (15) is expressed in the form of a function (16).

$$\begin{aligned} \dot{x}_1 &= f_1(x_2, \varphi, \delta) \\ \dot{x}_2 &= f_2(x_1, x_3, \varphi) \\ \dot{x}_3 &= f_3(x_2, x_3, \varphi) \end{aligned} \tag{16}$$

Linearizing (16) at the operating point, it is then expressed as a linear time invariant (LTI) state-space representation (17) with state vector $x_1 = [x_1, x_2, x_3]^{\mathrm{T}}$

$$\begin{aligned} \dot{\mathbf{x}} &= \mathbf{A}\mathbf{x} + \mathbf{B}\varphi + \mathbf{D}\delta \\ \mathbf{y} &= \mathbf{C}\mathbf{x} \end{aligned} \tag{17}$$

where the matrices **A**, **B**, and **D** are determined through Jacobian calculations as shown in (18). The calculation of (18) gives (19). Some parameters arise as a consequence of linearization, namely, x_1^*, x_2^*, x_3^*, and φ^* which represent the photovoltaic voltage, inductor current, capacitor voltage, and regulator input, respectively. These parameters are represented in Table 3.

$$\mathbf{A} = \begin{bmatrix} \frac{\partial f_1}{\partial x_1} & \frac{\partial f_1}{\partial x_2} & \frac{\partial f_1}{\partial x_3} \\ \frac{\partial f_2}{\partial x_1} & \frac{\partial f_2}{\partial x_2} & \frac{\partial f_2}{\partial x_3} \\ \frac{\partial f_3}{\partial x_1} & \frac{\partial f_3}{\partial x_2} & \frac{\partial f_3}{\partial x_3} \end{bmatrix}, \; \mathbf{B} = \begin{bmatrix} \frac{\partial f_1}{\partial \varphi} \\ \frac{\partial f_2}{\partial \varphi} \\ \frac{\partial f_3}{\partial \varphi} \end{bmatrix}, \; \mathbf{D} = \begin{bmatrix} \frac{\partial f_1}{\partial \delta} \\ \frac{\partial f_2}{\partial \delta} \\ \frac{\partial f_3}{\partial \delta} \end{bmatrix}$$

$$\mathbf{R} = \begin{bmatrix} 0 & -\frac{\varphi^*}{C_\alpha} & 0 \\ \frac{\varphi^*}{L} & 0 & \frac{1-\varphi^*}{L} \\ 0 & \frac{1-\varphi^*}{C_\beta} & -\frac{1}{RC_\beta} \end{bmatrix} \mathbf{x} + \begin{bmatrix} -\frac{x_2^*}{C_\alpha} \\ \frac{x_1^* - x_3^*}{L} \\ -\frac{x_2^*}{C_\beta} \end{bmatrix} \varphi + \begin{bmatrix} 1/C_\alpha \\ 0 \\ 0 \end{bmatrix} \delta \tag{18}$$

$$\mathbf{y} = \begin{bmatrix} 0 & 0 & 1 \end{bmatrix} \mathbf{x} \tag{19}$$

$\mathbf{C}(s\mathbf{I} - \mathbf{A})^{-1}\mathbf{B}$ from (19) is considered to obtain the transfer function (20), which expresses the input $\Phi(s)$ and the output $V_o(s)$ as follows:

$$G_{v_o\varphi} = \frac{V_o(s)}{\Phi(s)} = \frac{\begin{array}{c} -Rx_2^* LC_\alpha s^2 - C_\alpha R\left(x_1^* - x_3^*\right)(\varphi^* - 1)s + \\ R\varphi^* x_2^*(\varphi^* - 1) - Rx_2^* \varphi^{*2} \end{array}}{\begin{array}{c} C_\alpha C_\beta LRs^3 + C_\alpha Ls^2 + \\ \left(-C_\alpha R - C_\alpha R\varphi^{*2} + C_\beta R\varphi^{*2} + 2C_\alpha R\varphi^*\right)s + \varphi^{*2} \end{array}} \tag{20}$$

IV. UNCERTAINTY PROBLEM OF SYSTEM MODEL

The uncertainty of a model can be inherent in electronic components such as C_α, C_β, L, and R which means that these components have uncertain values due to various factors including, nominal component tolerances and operational conditions as stated in Table 2. Furthermore, uncertainty can also be inherent in the operating points of the system and input states, arising as a consequence of the linearization process. This includes the PV array voltage, output capacitor voltage, and inductor current.

Under ideal conditions, these operating points can be set to specific values. However, during operation, the operational voltage of the photovoltaic system is dynamic as a consequence of solar irradiance and temperature fluctuations. This means that the voltages across both the photovoltaic array and the input capacitor also undergo continuous variations. The operational current of the inductor adapts to the input voltage conditions based on the mode in which the converter is being operated. Consequently, the duty cycle values exhibit working range variability. The operating point uncertainty is displayed in Table 3.

According to (20), the system performance will degrade when confronted with variability. These conditions will

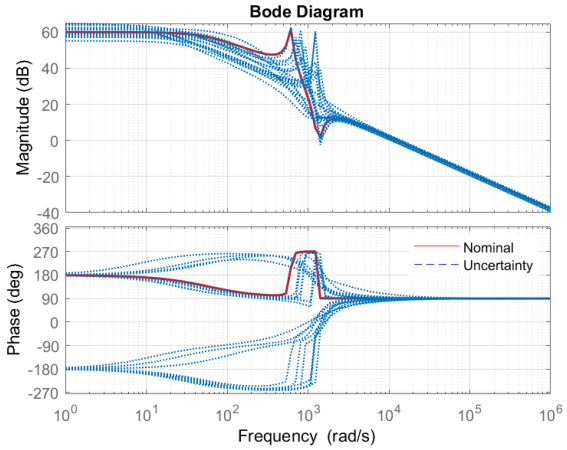

FIGURE 8. Frequency analysis of the nominal and uncertainty models.

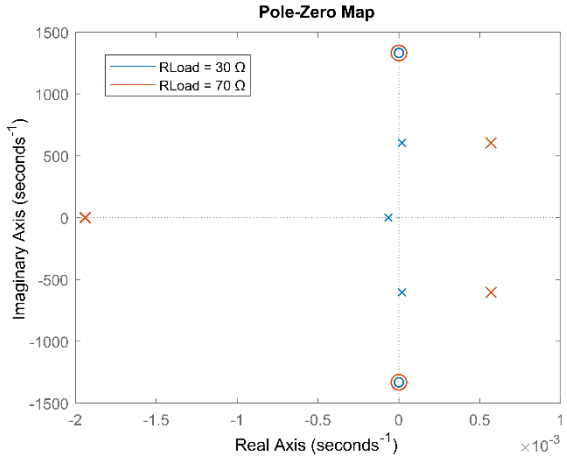

FIGURE 9. Pole zero plot of the open-loop system related to the load level.

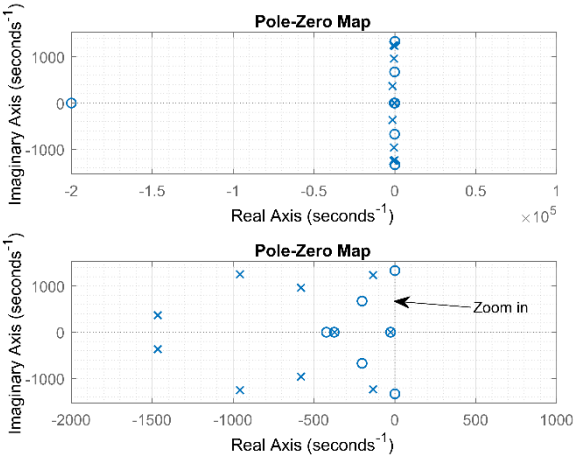

FIGURE 10. Pole zero plot after employing the robust control.

impact the transient and steady state of the system response, as shown in Fig. 8. The uncertainty in the parameters affects the cutoff frequency and dynamic response of the system. Additionally, changes in load also reduce system stability. This phenomenon can be observed from the pole zero map of the open loop system, as depicted in Fig. 9, where some poles are positioned to the right, resulting in system instability. When the load decreases, these poles approach the imaginary axis and consequently enhance the system oscillation.

V. ROBUST CONTROL DESIGN

The weighted mixed-sensitivity technique is one of the most robust H_∞ control approaches [59], [60]. A reference model together with a weighted mixed-sensitivity function as depicted in Fig. 11, is used for the close-loop control design to provide robustness against uncertainties resulting from solar irradiance fluctuations, temperature changes, nominal electronic component variability, and load variations, while simultaneously maintaining the reference performance.

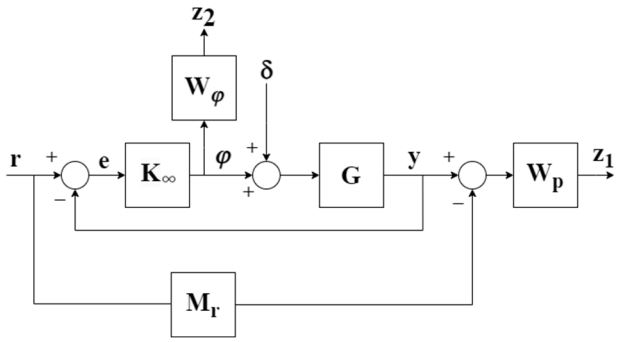

FIGURE 11. Closed-loop diagram with model reference.

According to Fig. 11, K_∞ is the control function, while W_p and W_φ are frequency-weighted functions. M_r is the model reference, $e = r - y$ is the error, φ is the control signal, z_1 is the output variable filtered by W_p, z_2 is the control variable filtered by W_φ, and δ is the disturbance. The weighting W_p is applied to ensure that the closed-loop system can track the reference model within the operating point range. W_φ is responsible for limiting the magnitude of the control action. Based on the control diagram, the augmentation system can be formulated as follows:

$$\begin{bmatrix} z_1 \\ z_2 \\ e \end{bmatrix} = [P(s)] \begin{bmatrix} r \\ \delta \\ \varphi \end{bmatrix} \tag{21}$$

where

$$[P(s)] = \begin{bmatrix} -M_r(s)W_p(s) & G(s)W_p(s) & G(s)W_p(s) \\ 0 & 0 & W_\varphi(s) \\ I & -G(s) & -G(s) \end{bmatrix} \tag{22}$$

and

$$\varphi = K_\infty e \tag{23}$$

S_i is the input sensitivity, and S_o is the output sensitivity.

$$S_i(s) = \frac{1}{1 + K_\infty(s)G(s)} \tag{24}$$

$$S_o(s) = \frac{1}{1 + G(s)K_\infty(s)} \tag{25}$$

T_i is the complementary input sensitivity, and T_o is the complementary output sensitivity.

$$T_i(s) = S_i(s)\,K_\infty(s)\,G(s) \tag{26}$$
$$T_o(s) = S_o(s)\,G(s)\,K_\infty(s) \tag{27}$$

According to [59], the linear fractional transformation (LFT) of $w \to z$ for $z = T_{zw}(P(s), K_\infty(s))\,w$ is given as follows:

$$z_1(s) = W_p(s)\,(T_o(s) - M_r(s))\,r(s) + W_p(s)G(s)S_o(s)d(s) \tag{28}$$
$$z_2(s) = W_\varphi(s)K_\infty(s)S_i(s)r(s) - W_\varphi(s)T_i(s)d(s) \tag{29}$$

Considering w as the input vector and z as the output vector in (30),

$$z = \begin{bmatrix} z_1 & z_2 \end{bmatrix}^T$$
$$w = \begin{bmatrix} r & d \end{bmatrix}^T \tag{30}$$

Therefore, the LFT statement fulfills Equation (31):

$$T_{zw} = \begin{bmatrix} W_p(s)\,(T_o(s) - M_r(s)) & W_p(s)S_o(s)G(s) \\ W_\varphi(s)K_\infty(s)S_i(s) & -W_\varphi(s)T_i(s) \end{bmatrix} \tag{31}$$

A controller K_∞ is developed such that it meets the minimum infinity norm as specified in condition (32) [61].

$$\|T_{zw}\|_\infty \le \gamma \tag{32}$$

which provides the conditions below:

$$\left\|W_p(s)\,(T_o(s) - M_r(s))\right\|_\infty \le \gamma$$
$$\to \overbrace{\|(T_o(s) - M_r(s))\|_\infty}^{C_1} \le \frac{\overbrace{\gamma}^{C_2}}{\left\|W_p(s)\right\|_\infty} \tag{33}$$
$$\left\|W_p(s)S_o(s)G(s)\right\|_\infty \le \gamma$$
$$\to \overbrace{\|S_o(s)G(s)\|_\infty}^{C_3} \le \frac{\overbrace{\gamma}^{C_4}}{\left\|W_p(s)\right\|_\infty} \tag{34}$$
$$\left\|W_\varphi(s)K_\infty(s)S_i(s)\right\|_\infty \le \gamma$$
$$\to \overbrace{\|K_\infty(s)S_i(s)\|_\infty}^{C_5} \le \frac{\overbrace{\gamma}^{C_6}}{\left\|W_\varphi(s)\right\|_\infty} \tag{35}$$
$$\left\|W_\varphi(s)T_i(s)\right\|_\infty \le \gamma \to \overbrace{\|T_i(s)\|_\infty}^{C_7} \le \frac{\overbrace{\gamma}^{C_8}}{\left\|W_\varphi(s)\right\|_\infty} \tag{36}$$

The conditions of (33), (34), (35), and (36) are aimed at improving the nominal good performance and stability, which means that the error e will be small even in the presence of input disturbances. The nominal model of the noninverting buck-boost converter G is augmented by $W_p(s)$ from the output side and $W_\varphi(s)$ from the input side in such a way that it forms a solution to the weighted mixed-sensitivity problem, as illustrated in Fig. 12.

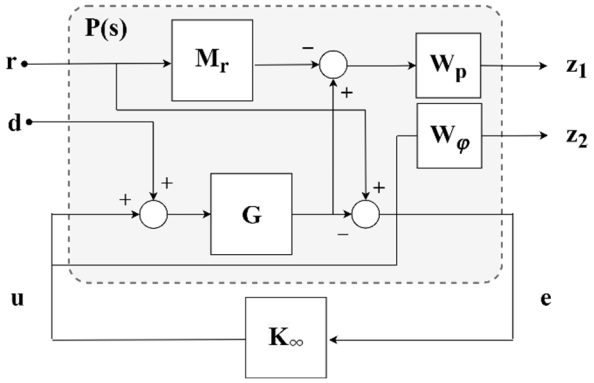

FIGURE 12. The considered structure for weighted mixed-sensitivity.

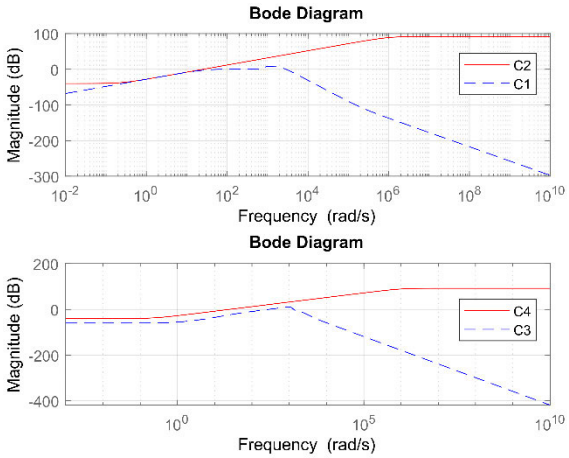

FIGURE 13. Frequency analysis of conditions (33) and (34).

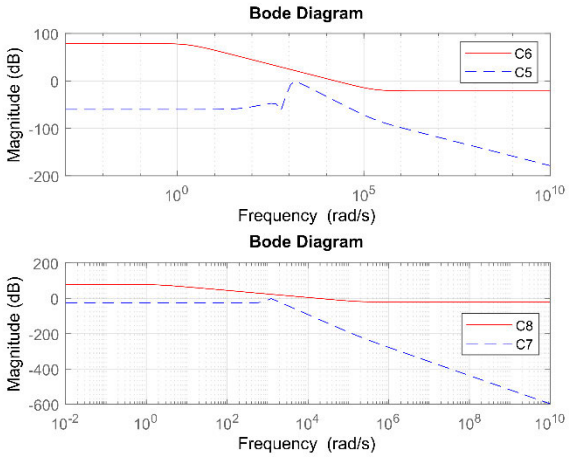

FIGURE 14. Frequency analysis of conditions (35) and (36).

Based on [33], the selected formats of $W_p(s)$ and $W_\varphi(s)$ are expressed in (37) and (39) respectively. In (37), M_1 is the minimum peak value of H_∞, the condition ω_1 provides the desired bandwidth, and ε_1 represents the tracking error

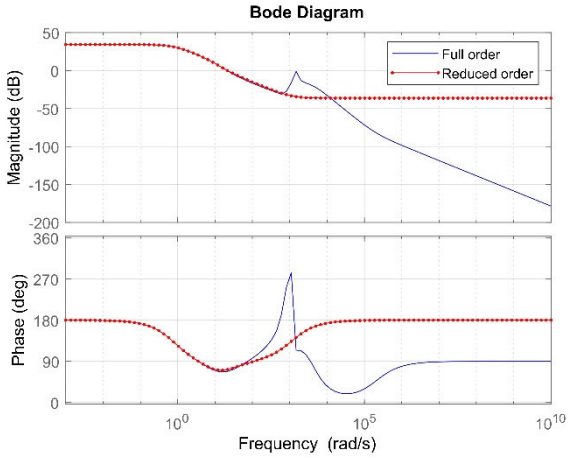

FIGURE 15. Frequency analysis of full-order and reduced-order controllers.

intended to be achieved at a steady state,

$$W_p(s) = \frac{\frac{s}{M_1} + \omega_1}{s + \omega_1 \varepsilon_1} \tag{37}$$

Considering the values of $M_1 = 5 \times 10^4$, $\omega_1 = 20$rad/s and $\varepsilon_1 = 8 \times 10^{-4.5}$, then (37) can be expressed as (38):

$$W_p(s) = \frac{5 \times 10^4 s + 20}{s + 5.1 \times 10^{-3}} \tag{38}$$

The format of $W_\varphi(s)$ is stated in (39). M_2 is the desired minimum H_∞ peak value. ω_2 is the desired closed-loop bandwidth. ε_2 represents the desired additional error at the steady state. The condition $W_\varphi^{-1}(s)$ should be achieved by the sensitivity function of the controller.

$$W_\varphi(s) = \frac{s + \frac{\omega_2}{M_2}}{\varepsilon_2 s + \omega_2} \tag{39}$$

Considering the values of $M_2 = 1$, $\omega_2 = 2.2 \times 10^4$rad/s and $\varepsilon_2 = 0.1$, (39) can be rewritten as (40):

$$W_\varphi(s) = \frac{s + 2.2 \times 10^4}{10^{-1} s + 2.2 \times 10^4} \tag{40}$$

The model reference M_r is introduced into the system as an ideal performance reference. In this context, M_r serves as the benchmark for an ideal system unaffected by disturbances. Moreover, it facilitates the assessment and restoration of system performance. The reference model is defined as a second-order system, which consequently simplifies the design of damping characteristics and time responses. The closed-loop system is designed to satisfy the second-order reference model with a damping coefficient of $\xi = 2$.

$$M_r = \frac{1}{T^2 s^2 + 2\xi T s + 1} \tag{41}$$

The procedure for obtaining the values of γ and controller K_∞ is realized using the toolbox MATLAB® software. The initial step is to define the component specifications and their uncertainty ranges in the system model of (15) using the toolbox *iconnec*. After that, the transfer function of weights $W_p(s)$ and $W_\varphi(s)$ is declared. Toolbox *sysic* is then utilized to drive the model and weight function for weighted mixed-sensitivity synthesis, as illustrated in Fig. 12. Finally, the values of the parameter γ and controller K_∞ are determined using the *hinfsyn* solver [62]. (42), as shown at the bottom of the next page.

The controller K_∞ is obtained by considering parameter $\gamma = 0.7924$, as shown in (42). Fig. 13 and Fig. 14 demonstrate that conditions (33) through (36) can be achieved, which means that the controller can mitigate the adverse effects of disturbance and maintain the control variable as if it were determined solely by the error value stated in (23). Fig. 13 shows that the output sensitivity S_o is located below W_p^{-1} which satisfies (33) and (34). This indicates that the requirements for tracking accuracy can be met. Similarly, the input sensitivity S_i of Fig. 14 is below W_φ^{-1}, which satisfies (35) and (36). This condition implies that the closed-loop system meets the robust performance criteria. Additionally, employing the robust controller (42) can shift all closed-loop poles to the left of the imaginary axis, as depicted in Fig. 10, thereby ensuring improved stability.

Equation (42) has a relatively high order. Considering a lower order provides computational benefits. This is achieved by applying the *balred* model order reduction solver [63] to Equation (42), resulting in a second-order function as shown in Equation (43). The results of the frequency response analysis of the full and reduced-order controllers are shown in Fig. 15. The magnitude and phase of the controller do not change at low frequencies. This is indicated by the controller's bandwidth, which is the amplitude when it reaches -3 dB and is nearly the same for both full-order and reduced-order controllers.

$$K_\infty(s) = \frac{-0.02s^2 - 17.6s - 343.47}{s^2 + 9.27s + 6.62} \tag{43}$$

The stages of the control design procedure described above can be summarized and illustrated in a flowchart, as depicted in Fig. 16.

VI. SIMULATION RESULT

The proposed control performance was verified by simulations conducted using the MATLAB/Simulink environment with the power system toolbox under various environmental conditions. The photovoltaic array was interfaced with the electric load by a noninverting buck-boost converter, establishing a closed-loop structure with a K_∞ controller (43), as depicted in Fig. 4. The simulation was implemented through four procedures. First, the simulation was carried out under the influence of varying irradiance levels. Second, the simulation was conducted under the influence of temperature variations. It was then validated under more challenging conditions, namely, under the simultaneous influence of changes in irradiance levels, temperature, and load. Finally, a performance comparison study was conducted between the proposed controller and a well-established proportional-integral-derivative (PID) controller.

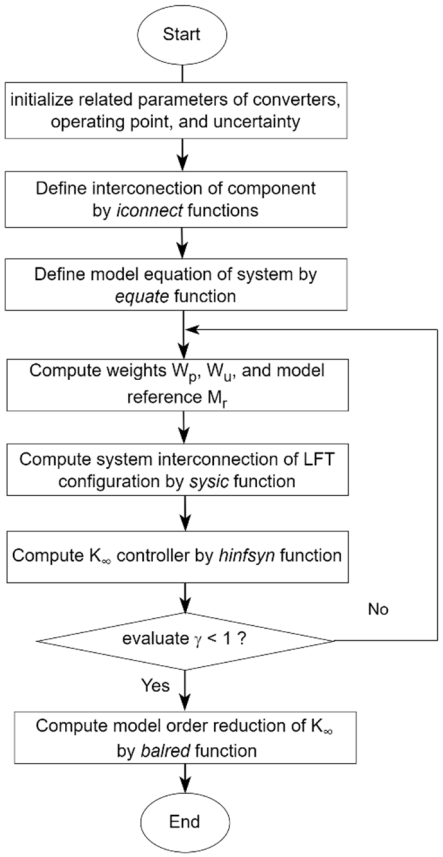

FIGURE 16. Control design procedure.

The photovoltaic array used in this test consists of four modules arranged in series and two modules arranged in parallel, resulting in a total configuration of eight modules. Each module contain 72 cells. The specifications of the PV array, converter, and operating point uncertainty are presented in Table 1, Table 2, and Table 3, respectively.

In the first evaluation, the irradiance changed every 0.1 second, resulting in a disturbance frequency of 10 Hz. The variations in irradiance levels are shown in Fig. 17. During the initial time interval, the photovoltaic array received irradiance of 300 W/m^2. Then, at 0.1 s, it increased to 600 W/m^2. Subsequently, at 0.2 s, the irradiance level increased to 1,000 W/m^2. After 0.3 s, the test was conducted using the same irradiance level as the previous interval but in a decreasing manner and concluded at 0.5 s. Throughout this test, the temperature and load were maintained at 25 °C and 50 Ω, respectively.

The control system performance in tracking of the PV voltage reference is verified in Fig. 18. The reference voltage

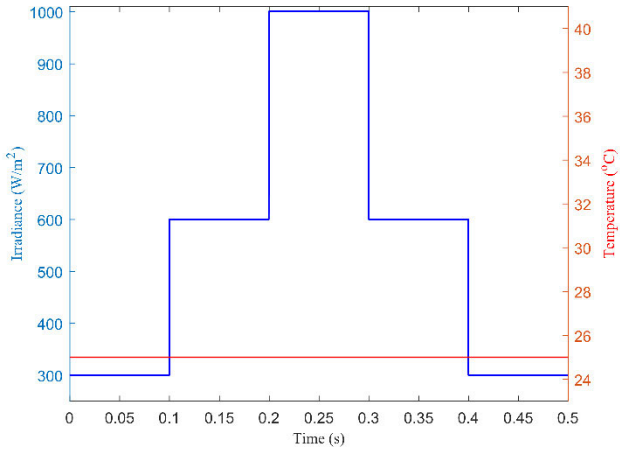

FIGURE 17. Varying level of irradiance.

is derived from the regression of the MPP voltage equation provided in (5), which is influenced by the incoming irradiance and temperature. The verification results under the conditions of the first test indicate successful MPP tracking with minimal oscillations. The rise time response to track takes approximately 0.018 seconds with an overshoot of approximately 0.329%, as shown in Fig. 18, and an average absolute steady-state error of approximately 0.286 Volt was achieved, as shown in Fig. 20. Furthermore, the performance of MPP tracking under irradiance changes is also successfully verified, as displayed in Fig. 19.

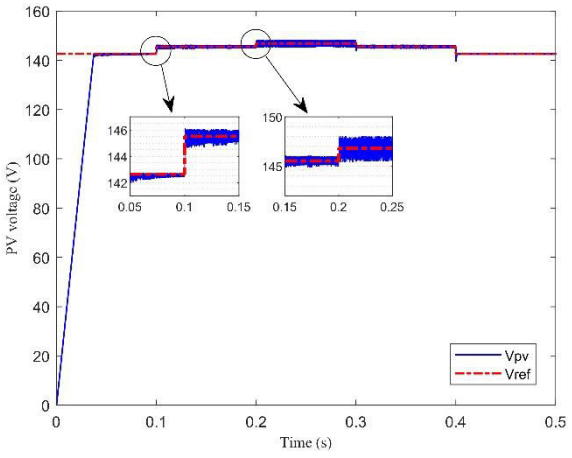

FIGURE 18. Voltage tracking under varying irradiance.

In the second test, the temperature changed every 0.1 second, resulting in a disturbance frequency of 10 Hz. The

$$K_\infty(s) = \frac{\begin{array}{c}-11.78s^6 - 2.371\times10^6 s^5 - 2.914\times10^9 s^4 - 2.383\times10^{12}s^3 \\ -1.144\times10^{15}s^2 - 2.138\times10^{17}s - 4.949\times10^{18}\end{array}}{\begin{array}{c}s^7 + 6677s^6 + 2.243\times10^7 s^5 + 1.985\times10^{10}s^4 \\ +3.967\times10^{13}s^3 + 1.34\times10^{16}s^2 + 1.328\times10^{17}s + 9.538\times10^{16}\end{array}} \tag{42}$$

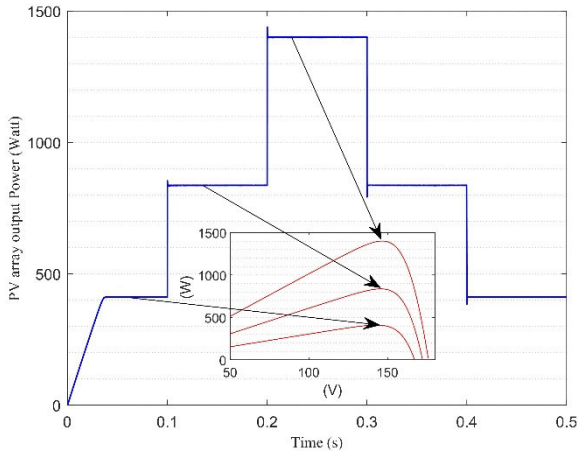

FIGURE 19. Power output under varying irradiance.

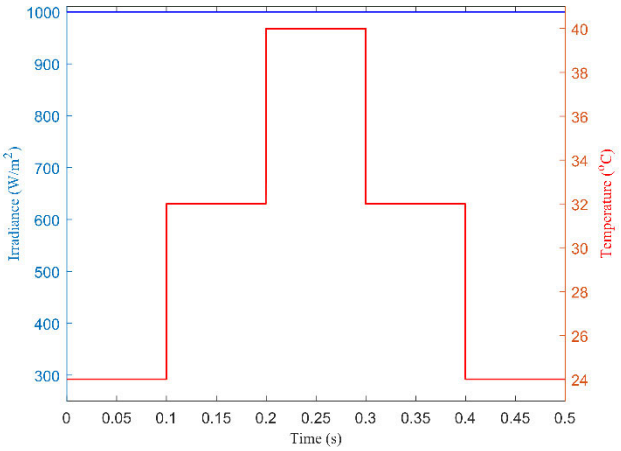

FIGURE 21. Varying temperature.

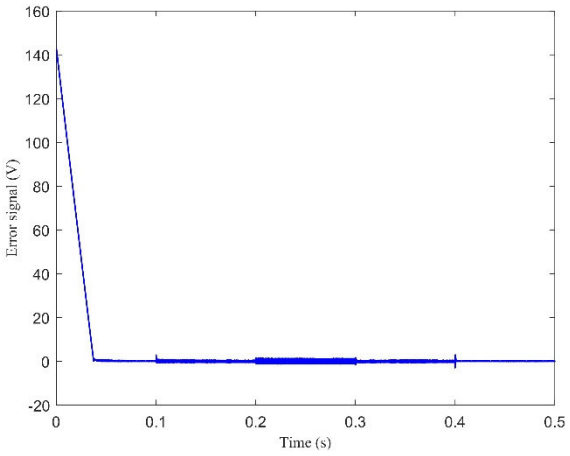

FIGURE 20. Error signal under varying irradiance.

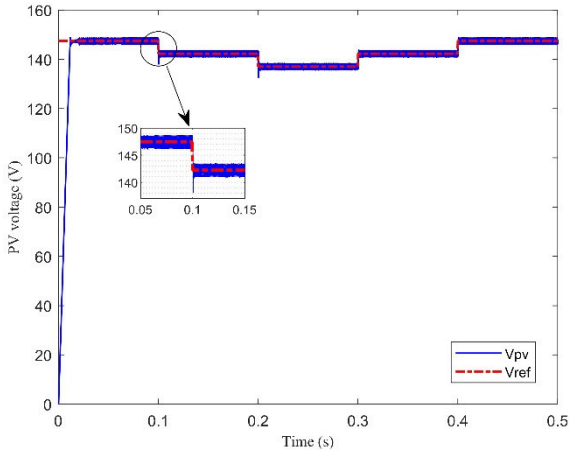

FIGURE 22. Voltage tracking under varying temperatures.

variations in temperature levels are shown in Fig. 21. During the initial time interval, the photovoltaic array was subjected to a temperature of 24 °C. Then, at 0.1 s, the temperature increased to 32 °C. Subsequently, at 0.2 s, the temperature rose again to 40 °C. After 0.3 s, the test continued using the same temperature level as the previous interval but in a decreasing manner and concluded at 0.5 s. Throughout this test, the temperature and load conditions were consistently maintained at 1000 W/m^2 and 50 Ω, respectively.

The performance of the proposed control system in tracking the reference voltage of the photovoltaic array is verified in Fig. 22. The verification results under the conditions of the second test indicate successful MPP tracking with minimal oscillations. The rise time response to track v_{mpp} took approximately 0.009 s with an overshoot of approximately 4.737% and achieved a small error of approximately 0.634 Volt, as shown in Fig. 24. Furthermore, the performance of MPP tracking under temperature changes was also successfully verified, as displayed in Fig. 23.

In the third testing scenario, irradiance changes followed the pattern of the first test, and temperature variations followed the scheme of the second test, as depicted in Fig. 25. In this test, the load values also changed as follows: the load was switched every 0.1 s, resulting in a disturbance frequency of 10 Hz. The variations in load levels are shown in Fig. 26.

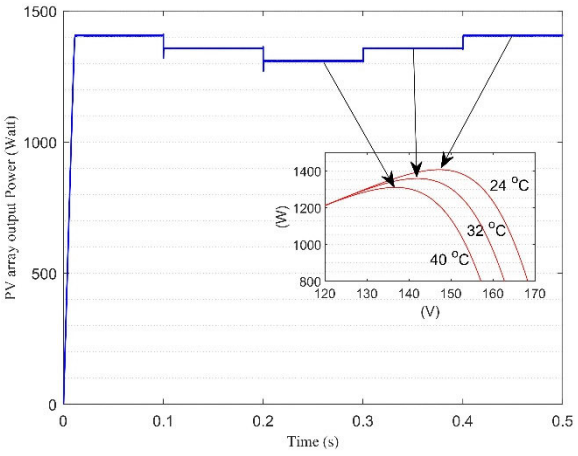

FIGURE 23. Power output under varying temperatures.

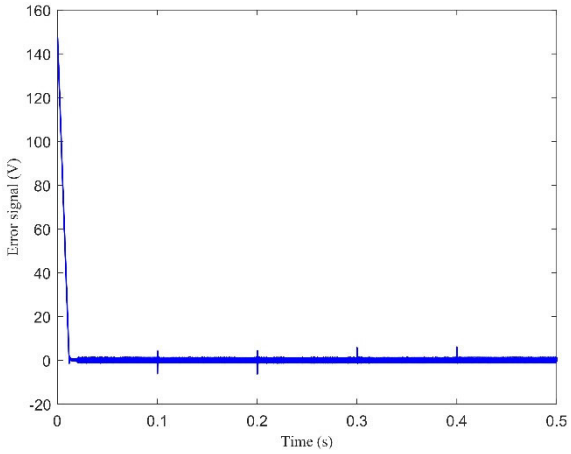

FIGURE 24. Error signal under varying temperatures.

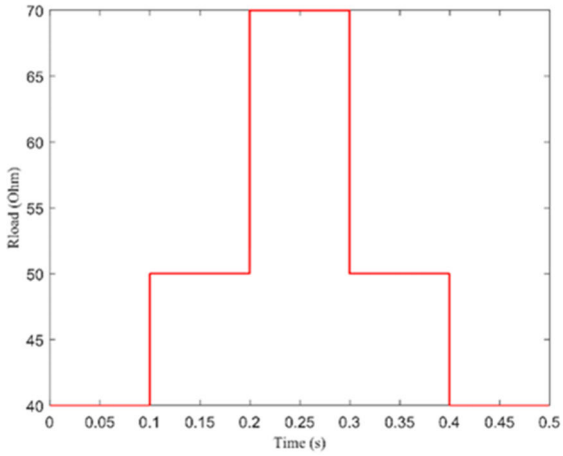

FIGURE 26. Varying levels of load.

During the initial time interval, the photovoltaic array was subjected to a load of 40 Ω. Then, at 0.1 s, it increased to 50 Ω. Subsequently, at 0.2 s, the load level rose again to 70 Ω. After 0.3 s, the test continued using the same load level as the previous interval but in a decreasing manner and concluded at 0.5 s.

The performance of the robust control system in tracking the reference voltage of the photovoltaic array is verified in Fig. 27. The verification results under the conditions of the third test indicate successful MPP tracking with minimal oscillation. The rise time response required approximately 0.027 s with an overshoot of approximately 0.535%, as shown in Fig. 27, and achieved an average steady-state error of approximately 0.3 Volt, as shown in Fig. 29. Furthermore, the performance of MPP tracking under temperature changes was also successfully verified, as displayed in Fig. 28.

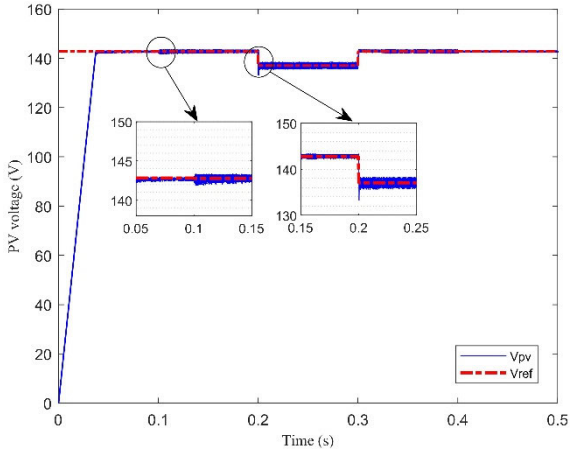

FIGURE 27. Voltage tracking under varying irradiance, temperature, and load.

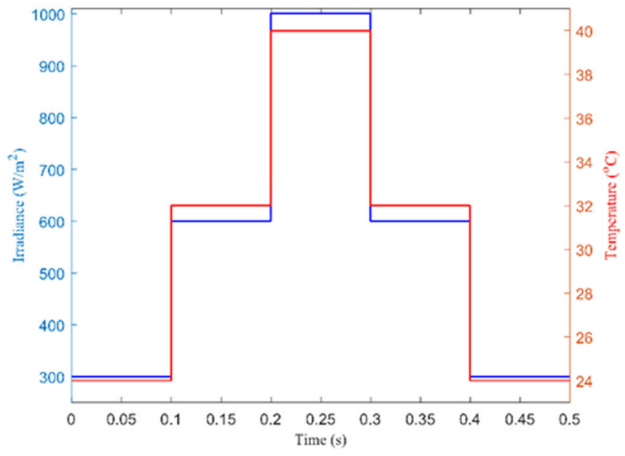

FIGURE 25. Varying irradiance and temperature levels.

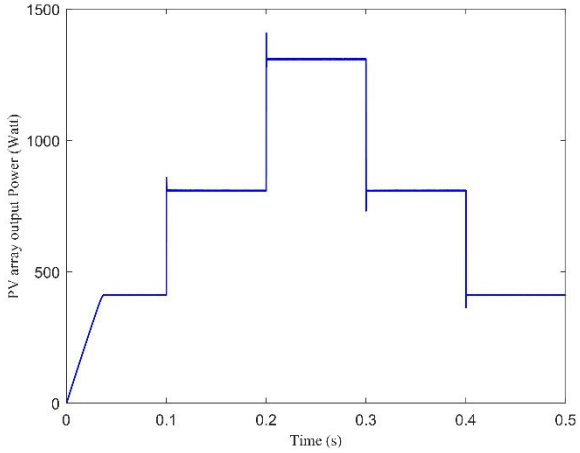

FIGURE 28. Power output under varying irradiance, temperature, and load.

The final testing scheme involved an evaluation study comparing the proposed controller and a proportional-integral-derivative controller under conditions in which irradiance, temperature, and load simultaneously changed.

The PID parameters were determined through a combined procedure involving the PID tuner of the MATLAB toolbox [63] and its improved adjustment. The PID tuner is

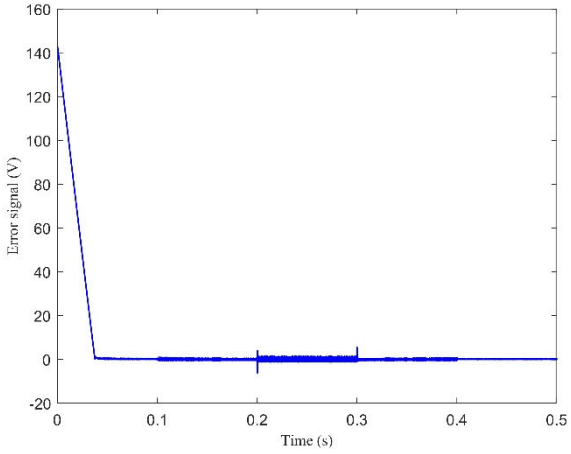

FIGURE 29. Error signal under varying irradiance, temperature, and load.

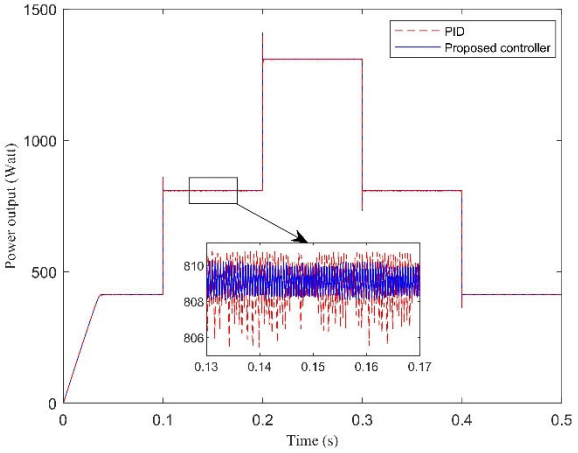

FIGURE 31. Power output comparison of the proposed controller and PID controller under varying irradiance, temperature, and load.

applied to the noninverting buck-boost converter, and this procedure yields the best PID parameter values of -10.275, -0.088, and $10^{-1.858}$. Each control method was tested by adopting a third testing scheme for irradiance, temperature, and load. The voltage tracking and power output data for each method are shown in Fig. 30 and Fig. 31, respectively. Closed-loop testing revealed a response speed of 27.034 ms and achieved a steady state in 16.373 ms. Furthermore, the closed-loop system also influenced the overshoot by 0.535% and the error toward the voltage reference in reaching the MPP by 0.212%. The proposed controller not only demonstrated fast voltage tracking but also exhibited smaller overshoot and oscillations. Furthermore, the power output generated by the performance of the designed controller also showed minimum oscillation.

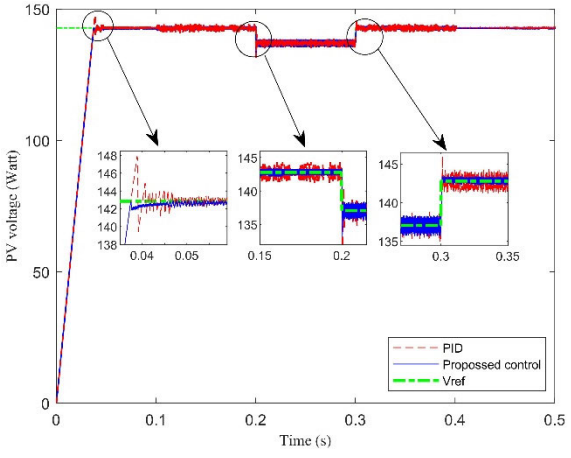

FIGURE 30. Voltage tracking comparison of the proposed controller and PID controller under varying irradiance, temperature, and load.

TABLE 1. PV array parameters.

Parameter	Value
Maximum power	1,400 W
Cells per module	72
Voltage at maximum power	146.52 V
Current at maximum power	9.56 A

TABLE 2. Converter parameters.

Parameter	Value	Uncertainty
Capacitor at input, C_i	480×10^{-6} F	±10%
Capacitor at output, C_o	810×10^{-6} F	±10%
Inductor, L	610×10^{-6} H	±10%
Resistive load, R	50 Ω	±40%
Switching frequency, f_s	200 kHz	-

TABLE 3. Operating points.

Parameter	Operating point	Uncertainty
x_1^*	146 Volts	±10%
x_2^*	20 Amperes	±10%
x_3^*	146 Volts	±10%
u^*	0.5	±90%

VII. EXPERIMENTAL RESULTS

In this section, an evaluation of the performance of the controller implemented in a laboratory-scale off-grid photovoltaic-based microcontroller is presented. The experimental setup of a prototype off-grid photovoltaic system is shown in Fig. 32, which involves several supporting devices: (A) a halogen lamp as light source, (B) a programmable load, (C) a temperature sensor, (D) a pyranometer, (E) a photovoltaic module, (F) an RS485 module, (G) a voltage sensor, (H) a microcontroller board, (I) a noninverting buck-boost converter, (J) PV and control monitoring, and (K) load monitoring. The design of the noninverting buck-boost converter and controller follows the block diagram depicted in Fig. 33. In this case, G represents the irradiance and T indicates the temperature as the basic data for determining the reference voltage v_{ref}. The error signal e is derived from the

difference between the voltage sensor v_{pv} and the reference voltage v_{ref}. Subsequently, the error signal becomes the input for the controller K_∞ to generate the control signal φ which is further processed into a PWM signal.

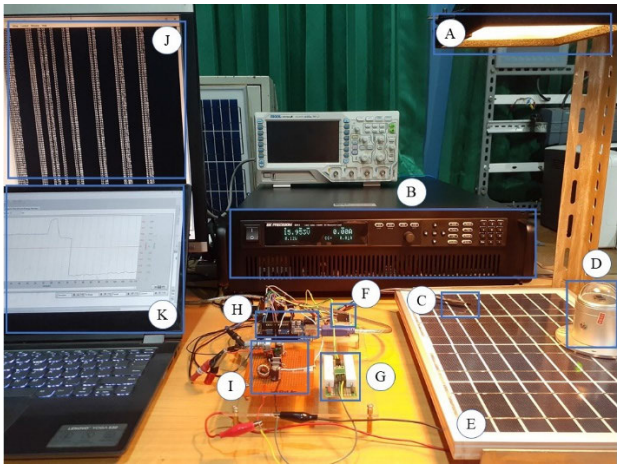

FIGURE 32. Developed experimental setup.

The proposed control system is integrated into the ATmega328P control board from Arduino. The board features a 10-bit analog-to-digital converter and 8-bit pulse width modulators. On the generator side, a photovoltaic module with a maximum power capacity of 10 Wp is utilized. This module is equipped with a PSP26474F3 pyranometer connected via the RS485 module to measure irradiance. Additionally, an LM35 sensor is used to measure the temperature of the photovoltaic module surface, and a voltage sensor is used to acquire input data for the noninverting buck-boost converter. The irradiance and temperature data are processed to determine the value of v_{ref} as the reference voltage for maximum power point tracking. The photovoltaic module is installed perpendicular to the light beam emitted from a halogen lamp. The lamp has a power rating of 500 W and is equipped with an adjustable dimmer to modify the light intensity. Furthermore, a 1,500 W programmable load BK Precision 8614 is connected on the output side. Any changes in irradiance and temperature are accompanied by gradual load change scenarios. The specifications of the photovoltaic module, the electronic components of the noninverting buck-boost converter, and the operating points for experimental verification are presented in Tables 4, 5, and 6, respectively.

The experiment is conducted with two scenarios. The first scenario involves irradiance and load disturbances, where the range of irradiance corresponds to one level of load change, as depicted in Fig. 34. The second scenario involves irradiance and load disturbances, where one irradiance range corresponds to three levels of load changes, as shown in Fig. 36. Temperature changes in both scenarios occur naturally due to the heat generated by the halogen spotlight and environmental temperature. The reference voltage v_{ref} for this off-grid photovoltaic system is shown in (44). The control equation K_∞ for the noninverting buck-boost converter with specifications from Table 5 is obtained by following the procedure shown in Fig. 16, and the resulting equation is shown in (45).

$$\begin{aligned} v_{ref} = {} & 16.7031 - 0.000104 \times \text{Temperature} \\ & + 0.004147 \times \text{Irradiance} \\ & - 0.000018 \times \text{Temperature}^2 \\ & - 0.000078 \times \text{Temperature} \times \text{Irradiance} \\ & - 0.000002 \times \text{Irradiance}^2 \end{aligned} \tag{44}$$

$$K_\infty(s) = \frac{3.407 \times 10^{-5} s^2 - 29.93s - 779.6}{s^2 + 9.015s + 6.716} \tag{45}$$

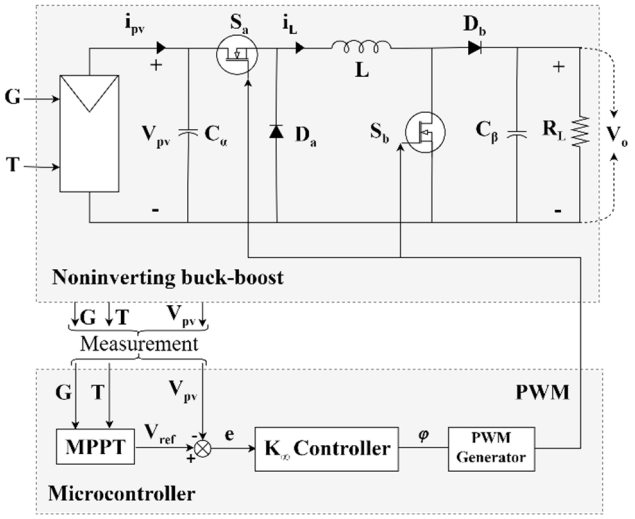

FIGURE 33. Diagram block of the noninverting buck-boost converter and controller.

In the first scenario, the converter on the input side is connected to the photovoltaic system. The irradiance and temperature conditions vary as shown in Fig. 34 (a). In the interval between 0 and 66 s, the photovoltaic system receives illumination with an irradiance of approximately 392.02 W/m^2. In the interval 67-135 s, the irradiance value then increases to approximately 723.28 W/m^2. Subsequently, in the range of 136-175 s, the irradiance decreases to approximately 425.08 W/m^2. It can be observed from the graph that the irradiance fluctuates due to the influence of environmental light. Similarly, the temperature on the surface of the photovoltaic system contributes to the heat generated by the halogen lamp and the environmental temperature. Meanwhile, on the output side, the noninverting buck-boost converter faces load variations under constant current load conditions as shown in Fig. 34 (b): in the interval between 0-66 seconds, it is 0.001 A, and in the interval between 67-135 s, it increases to 0.009 A. Subsequently, in the range of 136-175 s, the load decreases to 0.005 A.

The performance of the control system in dealing with this first test scenario can be evaluated in Fig. 35 (a). Shortly after the automatic mode was initiated, there was an increase in voltage approaching the reference value with a rise time of

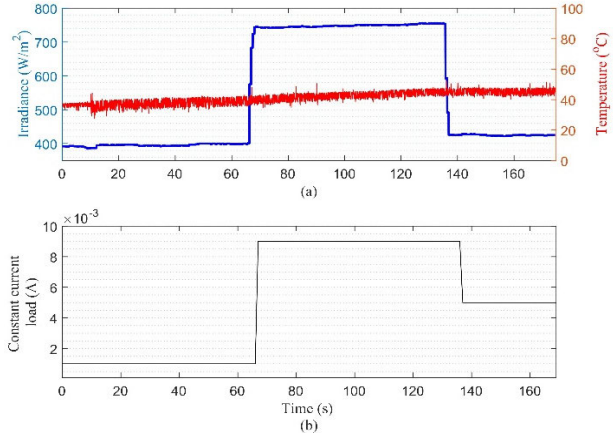

FIGURE 34. Testing conditions of the first scenario.

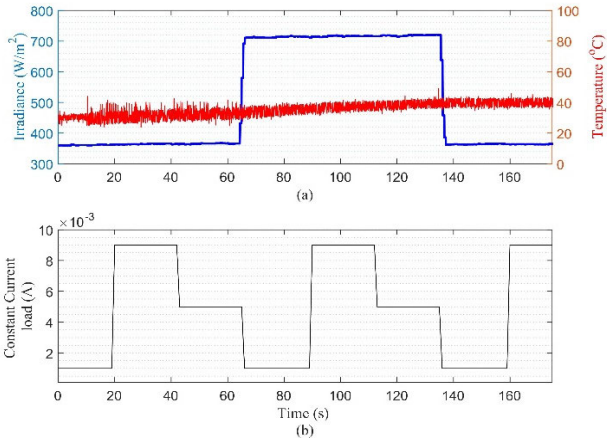

FIGURE 36. Testing conditions of the second scenario.

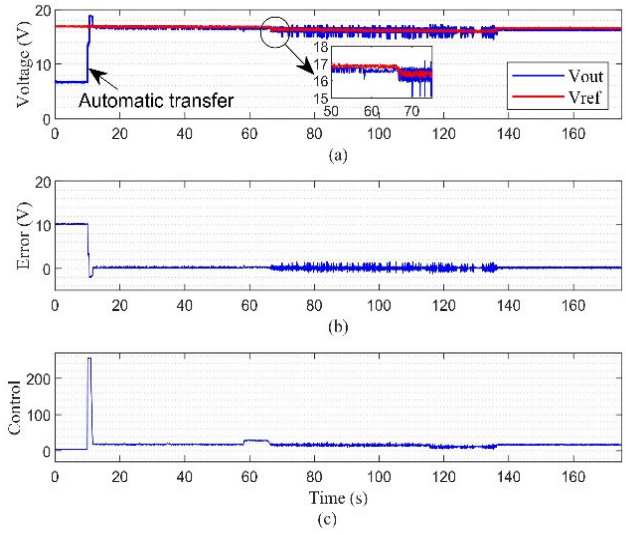

FIGURE 35. Proposed controller performance in the first scenario.

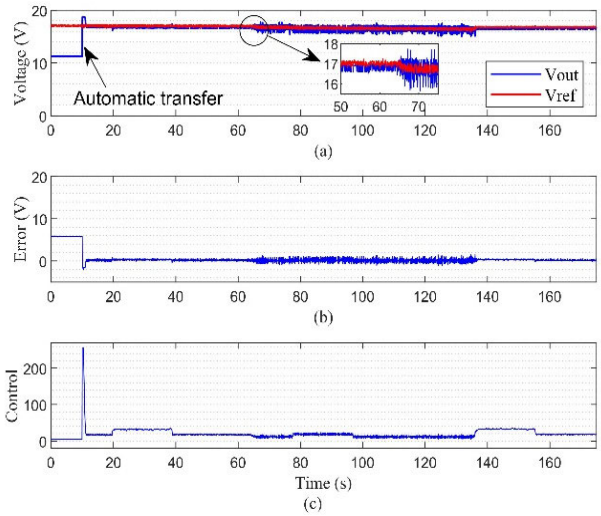

FIGURE 37. Proposed controller performance in the second scenario.

approximately 0.54 s. However, in its initial response, the voltage value exceeded the setpoint, resulting in an overshoot of approximately 10.75% within 0.91 s. Subsequently, it decreased closer to the setpoint value and reached steady state within 1.73 s. The magnified view shows that the voltage response can track sudden setpoint changes caused by irradiance and temperature shifts. The error condition in the steady state, as shown in Fig. 35 (b), indicates that the system response exhibits an average error of approximately 0.29 Volt, or equivalent to 1.76% for all test ranges.

In the second testing scenario, the converter on the input side was connected to the photovoltaic system. The irradiance and temperature conditions varied as shown in Fig. 36 (a). In the interval between 0 and 66 s, the photovoltaic system received illumination with an irradiance of approximately 363.54 W/m^2. In the interval of 67-135 s, the irradiance increases to approximately 714.52 W/m^2. Subsequently, in the range of 136-175 s, the irradiance decreased to approximately 363.84 W/m^2. It can be observed from the graph that the irradiance fluctuates due to the influence of environmental light. Similarly, the temperature on the surface of the photovoltaic system contributes to the heat generated by the halogen lamp and the environmental temperature. Meanwhile, on the output side, the noninverting buck-boost converter faces load variations under constant current load conditions, as shown in Fig. 36 (b). In the interval between 0-66 seconds, the system experiences three alternating load levels, each at 0.001 A, 0.009 A, and 0.005 A. This condition also applies at intervals of 67-135 seconds and 136-175 seconds.

The performance of the control system in managing this second test scenario can be evaluated in Fig. 37 (a). Shortly after the automatic mode is initiated, there is a voltage increase toward the reference value with a rise time of 0.01 seconds. However, in its initial response, the voltage exceeds the setpoint, resulting in an overshoot of approximately 9.24% within 0.90 seconds. Subsequently, the voltage gradually approaches the setpoint value and stabilizes within

1.33 seconds. The zoomed-in view illustrates that the voltage response can track sudden setpoint changes caused by shifts in irradiance and temperature. The error condition in a steady state, as shown in Fig. 37 (b), indicates that the system response exhibits an average error of approximately 0.31 Volt or approximately 1.87% for all test ranges.

In both aforementioned experimental scenarios, the proposed control system demonstrates a very short response time specifically, less than 1 second-in both test scenarios. When the voltage overshoot was less than 11%, in both trial scenarios, the experiments were consistently completed in less than 1 second. Furthermore, the settling time was less than 2 seconds, with a tracking error percentage less than 2%. The experimental results indicate that the proposed algorithm is implementable and delivers good performance in the hardware system of an off-grid photovoltaic-based noninverting buck-boost converter system.

TABLE 4. PV module parameters under the experimental conditions.

Parameter	Value
Maximum power	10 W
Cells per module	32
Voltage at maximum power	17.2 V
Current at maximum power	0.61 A

TABLE 5. Noninverting buck-boost parameters under the experimental conditions.

Parameters	Value	Uncertainty
Capacitor at input, C_i	100×10^{-6} F	±10%
Capacitor at output, C_o	330×10^{-6} F	±10%
Inductor, L	100×10^{-6} H	±10%
Constant current load	0.005 A	±80%
Switching frequency, f_s	400 kHz	-

TABLE 6. Operating points under experimental conditions.

Parameter	Operating point	Uncertainty
x_1^*	16 Volts	±10%
x_2^*	0.004 Ampere	±10%
x_3^*	16 Volts	±10%
u^*	127	±90%

VIII. CONCLUSION

In this paper, a weighted mixed-sensitivity control system was designed to track the reference voltage of the PV system as a reference to reach the MPP. The PV system was interfaced with an electric load by a noninverting buck-boost converter. To achieve the MPP of the PV array system, the controller modified the duty cycle of the PWM generator in the noninverting buck-boost converter, referencing the voltage setpoint derived from the regression plane. Robust stability and robust performance are verified with LFT norm conditions, where all conditions can be met, resulting in good system performance during testing under variations in irradiance, temperature, and load. A comparison with proportional-integral-derivative control was also performed. This demonstrates that the proposed controller performs better during variations in irradiance, temperature, and load levels.

REFERENCES

[1] O. M. Babatunde, J. L. Munda, and Y. Hamam, "A comprehensive state-of-the-art survey on hybrid renewable energy system operations and planning," *IEEE Access*, vol. 8, pp. 75313–75346, 2020, doi: 10.1109/ACCESS.2020.2988397.

[2] F. Lv and H. Tang, "Sustainable photovoltaic power generation spatial planning through ecosystem service valuation: A case study of the qinghai-tibet plateau," *Renew. Energy*, vol. 222, Feb. 2024, Art. no. 119876, doi: 10.1016/j.renene.2023.119876.

[3] K. Gholami, A. Azizivahed, A. Arefi, M. M. Rahman, M. R. Islam, L. Li, M. T. Arif, and M. E. Haque, "Hybrid uncertainty approach for management of energy storage-embedded soft open points in distribution grids," *J. Energy Storage*, vol. 87, May 2024, Art. no. 111394, doi: 10.1016/j.est.2024.111394.

[4] F. Saleh Al-Ismail, "A critical review on DC microgrids voltage control and power management," *IEEE Access*, vol. 12, pp. 30345–30361, 2024, doi: 10.1109/ACCESS.2024.3369609.

[5] M. Shafiullah, S. D. Ahmed, and F. A. Al-Sulaiman, "Grid integration challenges and solution strategies for solar PV systems: A review," *IEEE Access*, vol. 10, pp. 52233–52257, 2022, doi: 10.1109/ACCESS.2022.3174555.

[6] X. Zhou, Q. Liu, Y. Ma, and B. Xie, "DC-link voltage research of photovoltaic grid-connected inverter using improved active disturbance rejection control," *IEEE Access*, vol. 9, pp. 9884–9894, 2021, doi: 10.1109/ACCESS.2021.3050191.

[7] K. H. Lim, J. C. Kurnia, S. Roy, B. J. Bora, and B. J. Medhi, "Towards sustainable power generation: Recent advancements in floating photovoltaic technologies," *Renew. Sustain. Energy Rev.*, vol. 194, Apr. 2024, Art. no. 114322, doi: 10.1016/j.rser.2024.114322.

[8] Y. Ko, M. Andresen, K. Wang, and M. Liserre, "Modulation for cascaded multilevel converters in PV applications with high input power imbalance," *IEEE Trans. Power Electron.*, vol. 36, no. 9, pp. 10866–10878, Sep. 2021, doi: 10.1109/TPEL.2021.3065028.

[9] J.-S. Hwang, A. Khan, W.-J. Shin, J.-K. Seong, J.-G. Lee, Y.-H. Kim, and B.-W. Lee, "Validity analysis on the positioning of superconducting fault current limiter in neighboring AC and DC microgrid," *IEEE Trans. Appl. Supercond.*, vol. 23, no. 3, Jun. 2013, Art. no. 5600204, doi: 10.1109/TASC.2012.2228735.

[10] O. C. Zevallos, J. B. Da Silva, F. Mancilla-David, F. A. S. Neves, R. C. Neto, and R. B. Prada, "Control of photovoltaic inverters for transient and voltage stability enhancement," *IEEE Access*, vol. 9, pp. 44363–44373, 2021, doi: 10.1109/ACCESS.2021.3066147.

[11] M. Mao, L. Cui, Q. Zhang, K. Guo, L. Zhou, and H. Huang, "Classification and summarization of solar photovoltaic MPPT techniques: A review based on traditional and intelligent control strategies," *Energy Rep.*, vol. 6, pp. 1312–1327, Nov. 2020, doi: 10.1016/j.egyr.2020.05.013.

[12] H. Armghan, I. Ahmad, A. Armghan, S. Khan, and M. Arsalan, "Backstepping based non-linear control for maximum power point tracking in photovoltaic system," *Sol. Energy*, vol. 159, pp. 134–141, Jan. 2018, doi: 10.1016/j.solener.2017.10.062.

[13] F. Méndez-Díaz, B. Pico, E. Vidal-Idiarte, J. Calvente, and R. Giral, "HM/PWM seamless control of a bidirectional buck–boost converter for a photovoltaic application," *IEEE Trans. Power Electron.*, vol. 34, no. 3, pp. 2887–2899, Mar. 2019, doi: 10.1109/TPEL.2018.2843393.

[14] Z. Cabrane, J. Kim, K. Yoo, and M. Ouassaid, "HESS-based photovoltaic/batteries/supercapacitors: Energy management strategy and DC bus voltage stabilization," *Sol. Energy*, vol. 216, pp. 551–563, Mar. 2021, doi: 10.1016/j.solener.2021.01.048.

[15] C. Restrepo, B. Barrueto, D. Murillo-Yarce, J. Muñoz, E. Vidal-Idiarte, and R. Giral, "Improved model predictive current control of the versatile buck-boost converter for a photovoltaic application," *IEEE Trans. Energy Convers.*, vol. 37, no. 3, pp. 1505–1519, Sep. 2022, doi: 10.1109/TEC.2022.3183986.

[16] N. Obeidi, M. Kermadi, B. Belmadani, A. Allag, L. Achour, N. Mesbahi, and S. Mekhilef, "A modified current sensorless approach for maximum power point tracking of partially shaded photovoltaic systems," *Energy*, vol. 263, Jan. 2023, Art. no. 125618, doi: 10.1016/j.energy.2022.125618.

[17] R. Iskandar, E. Leksono, and E. Joelianto, "Q-learning hybrid type-2 fuzzy logic control approach for photovoltaic maximum power point tracking under varying solar irradiation exposure," *Int. J. Intell. Eng. Syst.*, vol. 14, no. 5, pp. 199–208, Oct. 2021, doi: 10.22266/ijies2021.1031.19.

[18] P. J. Antsaklis and X. D. Koutsoukos, "Hybrid systems: Review and recent progress," in *Software-Enabled Control, Information Technology for Dynamical Systems*. NJ, USA: IEEE Press, 2003, pp. 273–298, doi: 10.1002/047172288x.ch14.

[19] H. Y. Sutarto, A. Budiyono, E. Joelianto, and G. T. Hiong, "Switched linear control of a model helicopter," in *Proc. 9th Int. Conf. Control, Autom., Robot. Vis.*, Dec. 2006, pp. 1–8, doi: 10.1109/ICARCV.2006.345254.

[20] H. Lin and P. J. Antsaklis, "Hybrid dynamical systems: An introduction to control and verification," *Found. Trends Syst. Control*, vol. 1, no. 1, pp. 1–172, Jan. 2014, doi: 10.1561/2600000001.

[21] E. Joelianto and D. Williamson, "Stability of impulsive dynamical systems," in *Proc. 37th IEEE Conf. Decis. Control*, Mar. 1998, pp. 3717–3722, doi: 10.1109/CDC.1998.761787.

[22] M. S. Branicky, "Introduction to hybrid systems," in *Handbook of Networked and Embedded Control Systems*. Boston, MA, USA: Birkhäuser, 2005, pp. 91–116, doi: 10.1017/cbo9780511807930.002.

[23] E. Joelianto and D. Williamson, "Transient response improvement of feedback control systems using hybrid reference control," *Int. J. Control*, vol. 82, no. 10, pp. 1955–1970, Oct. 2009, doi: 10.1080/00207170902866120.

[24] N. Y. Megawati, E. Joelianto, and A. Budiyono, "Robust switched linear controller for multimode helicopter models," in *Proc. 2nd Int. Conf. Instrum. Control Autom.*, Bandung, Indonesia, Nov. 2011, pp. 152–156, doi: 10.1109/ICA.2011.6130147.

[25] N. Y. Megawati, E. Joelianto, and A. Budiyono, "Control of autonomous helicopter models with robust H_2-type switched linear controller," *Int. J. Appl. Math. Stat.*, vol. 35, no. 5, pp. 137–148, Jan. 2013.

[26] H. Ali, G. Magdy, and D. Xu, "A new optimal robust controller for frequency stability of interconnected hybrid microgrids considering non-inertia sources and uncertainties," *Int. J. Electr. Power Energy Syst.*, vol. 128, Jun. 2021, Art. no. 106651, doi: 10.1016/j.ijepes.2020.106651.

[27] Y. Ma, Q. Wang, M. Ye, and G. Lian, "Robust control for the hybrid energy system of an electric loader," *Machines*, vol. 11, no. 4, p. 454, Apr. 2023, doi: 10.3390/machines11040454.

[28] B. She, F. Li, H. Cui, J. Zhang, and R. Bo, "Fusion of microgrid control with model-free reinforcement learning: Review and vision," *IEEE Trans. Smart Grid*, vol. 14, no. 4, pp. 3232–3245, Jul. 2023, doi: 10.1109/TSG.2022.3222323.

[29] J. Zhai, X. Wu, S. Zhu, B. Yang, and H. Liu, "Optimization of integrated energy system considering photovoltaic uncertainty and multi-energy network," *IEEE Access*, vol. 8, pp. 141558–141568, 2020, doi: 10.1109/ACCESS.2020.3013396.

[30] J. Yang, H. Cui, S. Li, and A. Zolotas, "Optimized active disturbance rejection control for DC–DC buck converters with uncertainties using a reduced-order GPI observer," *IEEE Trans. Circuits Syst. I, Reg. Papers*, vol. 65, no. 2, pp. 832–841, Feb. 2018, doi: 10.1109/TCSI.2017.2725386.

[31] M. H. Sabzalian, K. A. Alattas, M. Aredes, A. K. Alanazi, H. M. Abo-Dief, A. Mohammadzadeh, S. Mobayen, B. W. França, and A. Fekih, "A new immersion and invariance control and stable deep learning fuzzy approach for power/voltage control problem," *IEEE Access*, vol. 10, pp. 68–81, 2022, doi: 10.1109/ACCESS.2021.3137719.

[32] M. Mehdi, S. Z. Jamali, M. O. Khan, S. Baloch, and C.-H. Kim, "Robust control of a DC microgrid under parametric uncertainty and disturbances," *Electric Power Syst. Res.*, vol. 179, Feb. 2020, Art. no. 106074, doi: 10.1016/j.epsr.2019.106074.

[33] M. Demirtas, H. Calgan, T. Amieur, and M. Sedraoui, "Small-signal modeling and robust multi-loop PID and H_∞ controllers synthesis for a self-excited induction generator," *ISA Trans.*, vol. 117, pp. 234–250, Nov. 2021, doi: 10.1016/j.isatra.2021.01.059.

[34] S. Hiti and D. Borojevic, "Robust nonlinear control for boost converter," *IEEE Trans. Power Electron.*, vol. 10, no. 6, pp. 651–658, Nov. 1995, doi: 10.1109/63.471284.

[35] S. Buso, "Design of a robust voltage controller for a buck-boost converter using /spl mu/-synthesis," *IEEE Trans. Control Syst. Technol.*, vol. 7, no. 2, pp. 222–229, Mar. 1999, doi: 10.1109/87.748148.

[36] W. Hernandez, J. de Vicente, and O. Sergiyenko, "H8 loop-shaping control of a buck-boost converter," in *Proc. IEEE Int. Conf. Ind. Technol.*, Via del Mar, Chile, Mar. 2010, pp. 1319–1323.

[37] E. Joelianto, "A robust DC-to-DC buckboost converter using PID hoo-backstepping controller," in *Proc. 5th Int. Conf. Power Electron. Drive Syst.*, Singapore, 2003, pp. 591–594, doi: 10.1109/peds.2003.1282912.

[38] M. Sitbon, S. Schacham, and A. Kuperman, "Disturbance observer-based voltage regulation of current-mode-boost-converter-interfaced photovoltaic generator," *IEEE Trans. Ind. Electron.*, vol. 62, no. 9, pp. 5776–5785, Sep. 2015, doi: 10.1109/TIE.2015.2434796.

[39] D. Gandini, P. Sorbellini, and M. Chiaberge, "Robust control architecture for waste heat harvesting with non-inverting buck-boost converter," in *Proc. 23rd Eur. Conf. Power Electron. Appl.*, Ghent, Belgium, Sep. 2021, pp. 1–10, doi: 10.23919/EPE21ECCEEurope50061.2021.9570715.

[40] D. Cortes-Vega and H. Alazki, "Robust maximum power point tracking scheme for PV systems based on attractive ellipsoid method," *Sustain. Energy, Grids Netw.*, vol. 25, Mar. 2021, Art. no. 100410, doi: 10.1016/j.segan.2020.100410.

[41] R. Keskin, I. Aliskan, and E. Das, "Robust fixed-order H_∞ controller synthesis for multi-phase converters with input voltage feed-forward," *J. Franklin Inst.*, vol. 360, no. 12, pp. 8251–8276, Aug. 2023, doi: 10.1016/j.jfranklin.2023.06.012.

[42] R. Devarapalli and B. Bhattacharyya, "A framework for H_2/H_∞ synthesis in damping power network oscillations with STATCOM," *Iranian J. Sci. Technol., Trans. Electr. Eng.*, vol. 44, no. 2, pp. 927–948, Jun. 2020, doi: 10.1007/s40998-019-00278-4.

[43] M. M. Farag, N. Patel, A.-K. Hamid, A. A. Adam, R. C. Bansal, M. Bettayeb, and A. Mehiri, "An optimized fractional nonlinear synergic controller for maximum power point tracking of photovoltaic array under abrupt irradiance change," *IEEE J. Photovolt.*, vol. 13, no. 2, pp. 305–314, Mar. 2023, doi: 10.1109/JPHOTOV.2023.3236808.

[44] A. Kchaou, A. Naamane, Y. Koubaa, and N. M'sirdi, "Second order sliding mode-based MPPT control for photovoltaic applications," *Sol. Energy*, vol. 155, pp. 758–769, Oct. 2017, doi: 10.1016/j.solener.2017.07.007.

[45] I. Shams, S. Mekhilef, and K. S. Tey, "Improved social ski driver-based MPPT for partial shading conditions hybridized with constant voltage method for fast response to load variations," *IEEE Trans. Sustain. Energy*, vol. 12, no. 4, pp. 2255–2267, Oct. 2021, doi: 10.1109/TSTE.2021.3088119.

[46] L. Callegaro, M. Ciobotaru, D. J. Pagano, and J. E. Fletcher, "Feedback linearization control in photovoltaic module integrated converters," *IEEE Trans. Power Electron.*, vol. 34, no. 7, pp. 6876–6889, Jul. 2019, doi: 10.1109/TPEL.2018.2872677.

[47] L. Callegaro, M. Ciobotaru, D. J. Pagano, E. Turano, and J. E. Fletcher, "A simple smooth transition technique for the noninverting buck–boost converter," *IEEE Trans. Power Electron.*, vol. 33, no. 6, pp. 4906–4915, Jun. 2018, doi: 10.1109/TPEL.2017.2731974.

[48] P. C. Santhosh Kumar, R. Naveenkumar, M. Sharifpur, A. Issakhov, M. Ravichandran, V. Mohanavel, N. Aslfattahi, and A. Afzal, "Experimental investigations to improve the electrical efficiency of photovoltaic modules using different convection mode," *Sustain. Energy Technol. Assessments*, vol. 48, Dec. 2021, Art. no. 101582, doi: 10.1016/j.seta.2021.101582.

[49] P. G. V. Sampaio and M. O. A. González, "Photovoltaic solar energy: Conceptual framework," *Renew. Sustain. Energy Rev.*, vol. 74, pp. 590–601, Jul. 2017, doi: 10.1016/j.rser.2017.02.081.

[50] L. Hernández-Callejo, S. Gallardo-Saavedra, and V. Alonso-Gómez, "A review of photovoltaic systems: Design, operation and maintenance," *Sol. Energy*, vol. 188, pp. 426–440, Aug. 2019, doi: 10.1016/j.solener.2019.06.017.

[51] S. B. Prakash, G. Singh, and S. Singh, "Modeling and performance analysis of simplified two-diode model of photovoltaic cells," *Frontiers Phys.*, vol. 9, pp. 1–9, Oct. 2021, doi: 10.3389/fphy.2021.690588.

[52] M. Premkumar, C. Kumar, and R. Sowmya, "Mathematical modelling of solar photovoltaic cell/panel/array based on the physical parameters from the manufacturer's datasheet," *Int. J. Renew. Energy Develop.*, vol. 9, no. 1, pp. 7–22, Feb. 2020, doi: 10.14710/ijred.9.1.7-22.

[53] Y. Chaibi, A. Allouhi, M. Malvoni, M. Salhi, and R. Saadani, "Solar irradiance and temperature influence on the photovoltaic cell equivalent-circuit models," *Sol. Energy*, vol. 188, pp. 1102–1110, Aug. 2019, doi: 10.1016/j.solener.2019.07.005.

[54] R. B. Bollipo, S. Mikkili, and P. K. Bonthagorla, "Hybrid, optimization, intelligent and classical PV MPPT techniques: Review," *CSEE J. Power Energy Syst.*, vol. 7, no. 1, pp. 9–33, Jan. 2021, doi: 10.17775/CSEE-JPES.2019.02720.
[55] H. F. Ahmed, M. S. E. Moursi, B. Zahawi, K. A. Hosani, and A. A. Khan, "Switching-cell buck–boost AC–AC converter with common-ground and noninverting/inverting operations," *IEEE Trans. Power Electron.*, vol. 36, no. 12, pp. 13944–13957, Dec. 2021, doi: 10.1109/TPEL.2021.3087811.
[56] M. Kermadi, Z. Salam, J. Ahmed, and E. M. Berkouk, "A high-performance global maximum power point tracker of PV system for rapidly changing partial shading conditions," *IEEE Trans. Ind. Electron.*, vol. 68, no. 3, pp. 2236–2245, Mar. 2021, doi: 10.1109/TIE.2020.2972456.
[57] M. Boukerdja, A. Chouder, L. Hassaine, B. O. Bouamama, W. Issa, and K. Louassaa, "H_∞ based control of a DC/DC buck converter feeding a constant power load in uncertain DC microgrid system," *ISA Trans.*, vol. 105, pp. 278–295, Oct. 2020, doi: 10.1016/j.isatra.2020.05.031.
[58] H. Armghan, M. Yang, M. Q. Wang, N. Ali, and A. Armghan, "Nonlinear integral backstepping based control of a DC microgrid with renewable generation and energy storage systems," *Int. J. Electr. Power Energy Syst.*, vol. 117, May 2020, Art. no. 105613, doi: 10.1016/j.ijepes.2019.105613.
[59] D.-W. Gu, P. H. Petkov, and M. M. Konstantinov, *Advanced Textbooks in Control and Signal: Robust Control Design With MATLAB*, 2nd ed. Berlin, Germany: Springer, 2012.
[60] R. F. Curtain and Y. Zhou, "A weighted mixed-sensitivity H_∞/-control design for irrational transfer matrices," *IEEE Trans. Autom. Control*, vol. 41, no. 9, pp. 1312–1321, Sep. 1996, doi: 10.1109/9.536500.
[61] R. Kumar, S. R. Mohanty, and M. K. Verma, "A robust damping control for battery energy storage integrated power systems to mitigate inter-area oscillations," *Int. J. Electr. Power Energy Syst.*, vol. 157, Jun. 2024, Art. no. 109885, doi: 10.1016/j.ijepes.2024.109885.
[62] G. Balas, R. Chiang, A. Packard, and M. Safonov, *Robust Control Toolbox™ User's Guide*. MA, USA: MathWorks, 2024, pp. 2–3.
[63] *Control System Toolbox Reference*, The MathWorks, MA, USA, 2018, pp. 2–41.

REZA FAUZI ISKANDAR received the B.Ed. degree in physics education from Indonesia University of Education (UPI), Bandung, Indonesia, in 2003, and the M.Sc. degree in instrumentation and control from the Institut Teknologi Bandung (ITB), Bandung, in 2010, where he is currently pursuing the Ph.D. degree in control systems for smart microgrid with the Engineering Physics Department. His main research interests include control and dynamical systems, microgrid and energy storage systems, energy management, artificial intelligence, and science education.

HANADI received the Bachelor of Science degree in physics from Mataram University, Indonesia. He is currently pursuing the M.Sc. degree with the Energy Management Systems Division, School of Industrial Engineering, Bandung Institute of Technology (ITB), Indonesia. His current research interests include photovoltaic systems, specifically in the development of a digital model for microgrids to predict PV output power based on edge device technology.

HARTONO received the B.E. degree in electrical engineering from Trisakti University, Indonesia. He is currently pursuing the master's degree in instrumentation and control graduate program with the Faculty of Industrial Technology, Bandung Institute of Technology (ITB), Indonesia. From 2014 to 2021, he was a Design Engineer of robotics and automation systems in the automobile manufacturing process with Toyota Indonesia production line and in several affiliate countries in Asia–Pacific region. His research interests include vehicle electrification and the development of battery management systems.

EDI LEKSONO received the bachelor's degree in engineering physics from the Institut Teknologi Bandung (ITB), Bandung, Indonesia, in 1983, the M.Sc. degree from Tokyo Institute of Technology, Tokyo, Japan, in 1990, and the Ph.D. degree from Keio University, Tokyo, in 1998. He is currently a Professor of sustainable energy system with the Engineering Physics Department, Faculty of Industrial Technology, ITB. His current research interests include energy management, microgrid systems, and energy storage systems.

ENDRA JOELIANTO (Senior Member, IEEE) received the bachelor's degree in engineering physics from the Institut Teknologi Bandung (ITB), Indonesia, in 1990, and the Ph.D. degree in engineering from The Australian National University (ANU), Australia, in 2002. He is currently a Professor with the Instrumentation, Control, and Automation Research Group, Faculty of Industrial Technology, ITB, and the Head of the Center for Sustainable Transportation Technology Development, ITB. His research interests include hybrid/discrete event control systems, advanced control, artificial intelligence, intelligent systems, cyber physical systems, intelligent transportation systems, and precision farming. He was recipient of several awards.